

Nanodevice Arrays for Peripheral Nerve Fascicle Activation Using Ultrasound Energy-harvesting

Michael Donohoe, *Member, IEEE*, Brendan Jennings, *Member, IEEE*, Josep Miquel Jornet, *Member, IEEE*, and Sasitharan Balasubramaniam, *Senior Member, IEEE*

Abstract—We propose the use of wireless, energy-harvesting, implanted nanodevice arrays with electrodes for selective stimulation of peripheral nerves in the human body. We calculate the input ultrasound energy and harvested power for single fixed-size nanowire-based nanodevices at different tissue depths and compare these with the current and voltage levels required for peripheral neural stimulation. We model the dimensioning of arrays of nanodevices, embedded in biocompatible tissue patches, to meet these neural stimulation requirements. Selectivity of activation of particular nerve bundles requires that the output voltage and current of the array can be varied to increase or decrease penetration into the neural tissue. This variation can be achieved by changing the energised area of the array and/or by decreasing the incident ultrasound power. However, the array must be implanted horizontally relative to the incident ultrasound as any tilting of the nanodevices will reduce the harvested energy. The proposed approach provides a longer-term implant solution for nerve stimulation that allows the patient greater freedom of movement than with embedded tethered electrodes.

Index Terms—Nerve stimulation, Nanoscale devices, Energy Harvesting, Ultrasound.

I. INTRODUCTION

Neural tissue activation relies on the use of electrical current to stimulate specific parts of the nervous system in order to treat neurological conditions (e.g., Parkinson’s Disease), nerve breakages resulting from accidents, or neural connectivity for prosthetics. Stimulation of motor nerves at present is carried out by externally powered electrodes placed on the skin surface (*transcutaneous*) or under the skin (*subcutaneous*) in closer proximity to muscles or nerves [1], [2]. Electrodes can be single points or multiple arrays with variable voltage and current control. The stimulus levels for these electrodes can be minimised by placing them as close as possible to the main nerve tissue that needs to be stimulated. One type of electrode, the cuff electrode, can be wrapped around larger nerves [3] to minimise the applied voltage and current levels. The majority of these solutions require implanted electrodes

M. Donohoe, B. Jennings and S. Balasubramaniam are with the Telecommunications Software & Systems Group (TSSG), Waterford Institute of Technology, Ireland. S. Balasubramaniam is also with the Dept. of Electronic and Communication Engineering, Tampere University of Technology, Finland. J. M. Jornet is with the University at Buffalo, State University of New York, USA. Email: mdonohoe@tssg.org, sasi.bala@tut.fi, bjennings@wit.ie, jmjornet@buffalo.edu.

This work is supported by the Finnish Academy Research Fellow programme under Project no. 284531. It is also partly funded by the Irish Higher Education Authority under the Programme for Research in Third Level Institutions (PRTL) cycle 5, which is co-funded by the European Regional Development Fund (ERDF), via the Telecommunications Graduate Initiative, and by Science Foundation Ireland via the CONNECT research centre (grant no. 13/RC/2077).

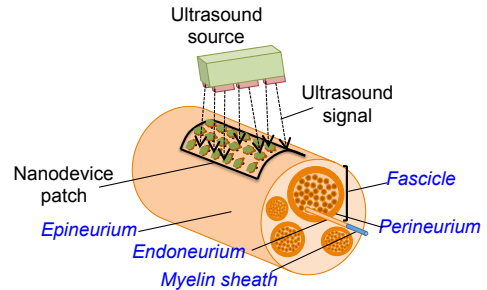


Fig. 1: Bio-compatible patch containing nanodevice array powered by externally generated ultrasonic waves. The array sends current pulses to stimulate specific *fascicles* (nerve fibre bundles).

that are wired to a power and control unit to deliver measured amounts of voltage and current [4] for functions such as deep brain stimulation, spinal cord stimulation, cochlear implants and cardiac pacemakers. A more advanced system for detecting brain activity and then transmitting locomotion signals wirelessly to the lower spinal cord is described by Capogrosso et al. [5]. Battery powered modules are used for signal detection and neural stimulation while external systems provide signal processing and protocol transmission. Smaller scale components and efficient powering would greatly enhance the deployment of such advanced prosthetics.

A major limitation of such solutions is the practicality of devices that can be implanted within patients and enable them to live a normal lifestyle. The challenges include (i) the ability to embed the device for longer-term deployment, where the devices can harvest energy from either the environment or an external source, avoiding the need for tethered wires, and (ii) ensuring that the device can be easily inserted into the nervous system and used to stimulate specific nerve bundles (e.g., along the elbow, spinal cord), while minimizing any stress on the tissue.

In this article, we address these challenges by proposing and modelling the use of nanoscale devices (“nanodevices”) that can be safely implanted into patients for the longer-term stimulation of selected peripheral nerve fascicles. The overall scenario is illustrated in Fig. 1, where a nanodevice array is embedded into a polymer-based patch of bio-compatible tissue [6], and placed against a nerve’s outer layer (*Epineurium*). The nanodevice harvests its energy from ultrasound waves that are emitted by a portable external source. The use of wireless powering and biocompatible materials will provide

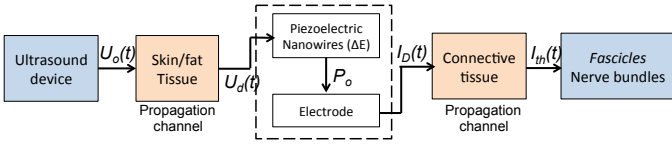


Fig. 2: Block diagram of end-to-end path from the ultrasound source through skin/fat and a nanodevice array resulting in the generation of an electrical current to stimulate the nerve fascicles.

greater longevity of components, though we do not have projections for the ultimate longevity of such a device. The patch must be both bio-compatible (to resist rejection, inflammation and bio-fouling) and non-degradable. Polymer-based bio-compatible materials specifically for substrates, structures and packaging are surveyed by Qin et al. [6]. They show how these materials can meet the requirements of implantable biosensors and describe different packaging methods. Polymer based packaging will also have acoustic impedance similar to human tissue (see §III-A) and will have a minimal impact on the performance of the array. The end-to-end power transfer process, illustrated in Fig. 2, shows the external ultrasound source emitting waves that bend the piezoelectric nanowires in each of the nanodevices in the patch. The harvested ultrasound energy is converted by the piezoelectric nanowires and releases an electronic pulse that stimulates nerve fascicles through an electrode. However, the nanodevices must harvest sufficient power for releasing the required threshold amount of current to stimulate specific nerve bundles. In previous work [7] we reported on an initial investigation of the use of ultrasounds to power subcutaneous nanowire-based nanodevices. That investigation showed how lower ultrasound frequencies provided better tissue penetration and more energy per cycle to bend nanowires. Here we extend that work by (i) calculating the output voltage and current of a nanodevice relative to the input ultrasound intensity and (ii) modelling the use of coupled nanodevices for selective neural stimulation particularly in the *fascicles* of the peripheral nerves of the wrist and forearm that control arm and hand movements: the *radial*, *median* and *ulnar*. The main competitive advantage of our proposed approach, based on the use of a synthetic patch array composed of nanodevices for stimulation, is the ability to stimulate nerve fascicles at different depths by varying the intensity of the incident ultrasound, or spatially targeting specific nanodevices on the patch. The piezoelectric nanowires can respond to lower ultrasound frequencies that can penetrate through a greater depth of tissue than higher frequencies.

The article is organised as follows: the architecture of energy-harvesting nanodevices using ultrasounds is outlined in §II; the transmission of ultrasound energy through human tissue and the power output of nanodevices is analysed in §III; the deployment for neural stimulation is modelled in §IV; and our conclusions are presented in §V.

II. NANODEVICE ENERGY HARVESTING

Our proposed nanodevice must convert incident ultrasounds into mechanical vibrations and then into piezoelectric energy

(Fig. 2). There are two main methods for harvesting ultrasounds: resonant *piezoelectric crystals* or vibrating *piezoelectric nanowires*. The size of a resonant crystal depends on the frequency of the ultrasound: the higher the frequency, the thinner the crystal. The powering of sensors embedded in tissue using resonant *lead zirconate titanate* (*PZT*) crystals has previously been investigated by Ozeri and Schmilovitz [8], using a frequency of 673 kHz. These devices are at a macro scale (cm^2) and not suitable for the miniature devices that we are targeting for our patch. A cuff electrode powered by a PZT crystal, operating at 1 MHz was also demonstrated by Larson and Towe [9]. Simple half-wave rectification of the output AC voltage with a single diode provided a stimulus pulse to the sciatic nerve of a rat. The output power and successful operation depend critically on the positioning and alignment of the crystal, which could easily be changed in a live body. The use of micro-scale resonant crystals (“neural dust”) for neural recording using ultrasound powering and backscatter was proposed by Seo et al [10]. The recording principle has been demonstrated for peripheral nerves [11] though the available components are at millimetre scale at present. For smaller scale operation, an energy harvesting resonant crystal would have dimensions in the micrometre scale, which would imply a resonant frequency in the 10 MHz or greater range; such a high frequency of ultrasound would be strongly absorbed by human tissue (see §III-A) so miniature resonant crystal harvesters could only be deployed at very shallow skin depths (e.g., 2 mm). Therefore, for deeper penetration using lower ultrasound frequencies, we consider piezoelectric *zinc oxide* (*ZnO*) nanowires that can vibrate in response to a range of ultrasound frequencies [7] and produce variable amounts of current and voltage.

A. Piezoelectric ZnO Nanowires

We use an analytical perturbation model for bending a *ZnO* nanowire developed by Gao and Wang [12]. The nanowire is modelled as a thin cylindrical rod with a specific modulus of elasticity (Young’s modulus). Bending a nanowire requires the application of a force that is countered by the elasticity of the nanowire. If a constant force F is applied until a bending before discharge y_m (as depicted in Fig. 3) is achieved, then the balance of forces is as follows:

$$F = \frac{3YIy_m}{L^3}. \quad (1)$$

In this case Y is the nanowire’s Young’s modulus, I is the area moment of inertia and L is the nanowire length. The bending is directly proportional to the applied force. The energy (work) ΔE required to bend the nanowire by an amount y_m is:

$$\Delta E = \frac{3YIy_m^2}{2L^3}. \quad (2)$$

The work is proportional to the square of the displacement. The voltage V is approximately linear over the range of applied forces, as analysed by Hinchet et al. [13] and can be expressed as:

$$V = G'y_m. \quad (3)$$

TABLE I: Force, displacement, work and voltage for bending a nanowire.

Force (nN)	Displacement (nm)	Work (fJ)	Voltage (V)
60	109	3.274	± 0.212
80	146	5.821	± 0.284
90	164	7.36	± 0.319
100	182	9.09	± 0.354

The parameter G has units of volts/nanometre and is a constant for specific values of diameter and length. Values for force, displacement, work and voltage (from (1), (2), (3)) for bending a nanowire that is 50 nm in diameter, 600 nm long and has a Young's Modulus of 129 GPa [12] are shown in Table I. The value of G is 1.9×10^{-3} V/nm. The work required for bending is of the order of femtojoules and the magnitude of bending is sufficient to deliver a piezoelectric energy output.

The use of ZnO nanowires for energy harvesting was proposed by Wang and Song [14] for delivering a periodic DC voltage and current. The nanowires in this type of DC nanodevice are fixed at one end to a substrate while the other end is free and can bend to touch a specially engineered corrugated (zigzag) electrode. External vibrations push the substrate and harvesting electrode together and hence bend the nanowires. The bent nanowire then has a stretched side with a positive charge and a compressed side with a negative charge. The negative charge is released when the compressed surface of the bent nanowire touches the electrode. Systematically bending the nanowires produces a unidirectional current and negative voltage that's collected by the electrode, as shown in Fig. 3. The zigzag electrode of the Wang device is made from platinum-coated silicon with parallel etched trenches. The substrate is made from a flexible polymer (preferably biosafe) coated with a thin film of gold. Aligned nanowire arrays can be grown on such a flexible substrate to match up with the trenches on the electrode. Spacing between the substrate and the electrode is provided by polymer strips that can be sealed if the device is to be immersed in liquid.

The maximum potential (voltage) at the nanowires surface is directly proportional to the bending and inversely proportional to the length-to-diameter aspect ratio. The bending creates a piezoelectric negative potential between the upper zigzag electrode and the lower substrate.

B. Ultrasound Energy-harvesting Nanowires

The overall power harvesting capability depends on: (i) the amount of bending the nanowires are subjected to; (ii) the bending events per second (frequency); and (iii) the nanowires per unit area (density). Ultrasound is once source of external vibration that can be used for energy harvesting. Ultrasound vibrations effectively push the electrode and substrate together at the frequency of the ultrasound. This dynamic distortion of the device causes the nanowires to bend but they do not resonate at the ultrasound frequency. Where ultrasound is used as a source of vibrational bending, the energy per cycle will determine the amount of bending while the ultrasound frequency will determine the quantity of bends per second.

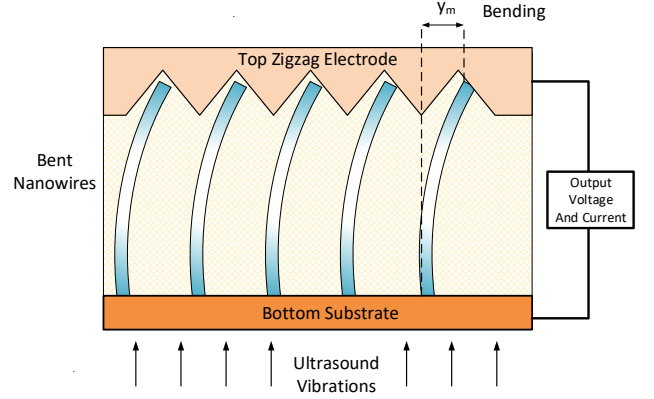


Fig. 3: Energy harvesting from bent nanowires using a corrugated top electrode and a conducting substrate. Vibrations push the bottom substrate towards the top electrode, causing the nanowires to bend and generate a negative potential due to the piezoelectric effect.

In order to demonstrate vibrational activation, a 2 mm^2 nano-generator using ZnO nanowires and powered by ultrasounds was developed by Wang et al. [15]. The device was immersed in water and subjected to ultrasound excitation at 41 kHz. The output current and voltage values were recorded as noisy square waves but the input intensity of the ultrasound was not recorded, making it difficult to assess the efficiency. The same group carried out similar ultrasound energy-harvesting tests in biofluids [16] that included coupling three devices in parallel and then in series to demonstrate boosting current and voltage. The square-wave output of these devices was as a result of (i) an inbuilt diode characteristic that delivered current in one direction only and (ii) capacitive effects in the contact between the nanowire and the electrode that helped spread the discharge of piezoelectricity through the electrode. The developers theorise that if all nanowires participated in current production, through better alignment and more uniform length, the result would be a much improved square wave DC output. Based on these considerations we model the output of a nanodevice as a DC square wave with no requirement for rectification and hence no additional power consumption or performance degradation.

We now compare the energy (work) levels for bending a nanowire (ΔE) as shown in Table I with the energy that can be delivered to a nanowire by ultrasounds.

III. ULTRASOUND AS AN ENERGY SOURCE

The ultrasound intensity used in our calculations is based on a maximum value of 720 mW/cm^2 , which is in line with medical recommendations [17]. In our computations, we use three different power intensities: (i) the initial intensity emanating from the ultrasound source (U_o); (ii) the ultrasound intensity entering the nanodevice following penetration through tissue layers (U_d); and (iii) the piezoelectric power intensity emerging from the nanodevice (P_o). We now model

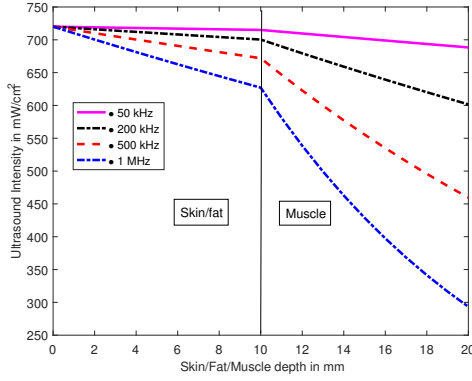


Fig. 4: Plot of Ultrasound Intensity vs Skin/Fat and Muscle Depth. The rate of absorption is significantly higher for denser muscle tissue in comparison to the less dense skin/fat.

the ultrasound intensity entering the nanodevice; §III-C models the power emerging from the nanodevice.

A. Ultrasound Absorption and Reflection in Human Tissue

Externally applied ultrasound will penetrate initially through several layers of human skin tissue. For peripheral nerve stimulation, the nanodevice would be embedded centimetres deep in subcutaneous fat. An ultrasonic beam of frequency f MHz with an initial intensity of U_o penetrating to a depth of d cm will have a resultant intensity of U_d :

$$U_d = U_o 10^{-(\alpha f d / 10)}. \quad (4)$$

The absorption coefficient α , expresses the power loss and has a value of 0.6 dB/cm/MHz for skin/fat and 1.8 dB/cm/MHz for muscle [17]. Figure 4 presents the ultrasound intensity with respect to tissue depth (U_d) and is based on (4), where the ultrasound attenuation is calculated through 10mm skin/fat and then 10mm muscle for four different ultrasound frequencies. The higher ultrasound frequencies are more strongly absorbed compared to lower frequencies, particularly in the denser muscle tissue.

Acoustic reflections at tissue interfaces (e.g., between fat and muscle) are caused by differences in *acoustic impedance* (the density of the tissue multiplied by the speed of sound); the unit of acoustic impedance is the Rayl ($\text{kg}\cdot\text{s}^{-1}\cdot\text{m}^{-2}$). The reflection at an air/human tissue interface would result in up to 99% of the ultrasound being reflected because of the large difference in the acoustic impedance [17] (429 Rayl for air, 1.4 MRayl for skin/fat). Consequently there should be no air gap between an ultrasound transducer and human tissue. For our nanodevice array, the acoustic impedance of the synthetic patch and the nanodevice substrate should match the acoustic impedance of body tissue as closely as possible.

B. Ultrasound Cycle Energy

Initially, we model a single nanodevice that is perpendicular to the ultrasound vibrations (no tilt) and hence can intercept the maximum amount of ultrasound energy. The input intensity is fixed at 720 mW/cm^2 , or $7.2 \times 10^{-9} \text{ W}/\mu\text{m}^2$, and the intensity

at different depths is calculated using (4). At a fixed density of m nanowires per μm^2 , the energy per nanowire per cycle, E_{nw} , at an ultrasound frequency of K cycles per second and intensity of $U_d \text{ W}/\mu\text{m}^2$ is calculated as follows:

$$E_{nw} = \frac{U_d}{mK}. \quad (5)$$

At 50 kHz the energy level is from 7.1 fJ to 6.7 fJ at 1cm and 10cm depth, respectively. The energy per cycle per nanowire at 1 MHz is initially over 20 times lower than at 50 kHz (0.03 fJ) and decreases more rapidly with depth. This means that the magnitude of 50 kHz ultrasound cycle energy per nanowire is comparable to the nanowire bending energies shown in Table I, but the 1 MHz cycle energies are too low to provide sufficient bending. Consequently, we will assume the use of ultrasound at a frequency of 50 kHz to power our nanodevices. By using a lower ultrasound frequency with lower tissue absorption and short-duration ($100 \mu\text{s}$) infrequent pulses of ultrasound (See §IV-A) we will minimise any possibility of tissue or nanodevice heating.

Maximum ultrasound power will be transferred to a nanodevice if the incident beam is perpendicular to the device substrate and hence strike the full nanodevice area. If a nanodevice is tilted at an angle to the ultrasound source, then the incident intensity will be reduced [18]. A nanodevice tilted at an arbitrary angle can be modelled as a combination of a horizontal tilt and a vertical tilt. If U_d is the intensity of a beam at a depth of d cm and a nanodevice is tilted at an angle θ in the horizontal plane and an angle ϕ in the vertical then the resulting intensity on the surface, U_r is:

$$U_r = U_d \cos\theta \cos\phi. \quad (6)$$

A plot of the ultrasound intensity at a skin/fat depth of 5 mm against varying horizontal and vertical tilt angles (0° to 90°) is shown in Fig. 5. The maximum intensity is 717 mW/cm^2 and drops steeply even for relatively small horizontal and vertical angles (e.g. 15°). Consequently the level of tilt must be minimised if a threshold intensity needs to be maintained to activate a nanodevice.

C. Power Output Analysis

The total output energy of a nanodevice depends on (i) the energy of the incident ultrasonic wave; (ii) the harvesting area; (iii) piezoelectric efficiency of the nanowires; (iv) absorption or reflection of ultrasound within the nanodevice; and (v) the fraction of nanowires that contribute to the electrical output. The input energy levels range between 5.82 fJ (bending force of 80 nN) and 9.09 fJ (bending force of 100 nN) per nanowire as shown in Table I. The DC *ZnO* nanodevice in [14] had a measured average output energy per nanowire of approximately 0.05 fJ, though this did not use ultrasound. A comparison with input energy levels suggests a conversion efficiency of between 0.8% and 0.55%. The output power P_o is computed from the nanodevice area A , the incident ultrasound intensity U_r and the conversion efficiency e , and is represented as follows:

$$P_o = AU_r e. \quad (7)$$

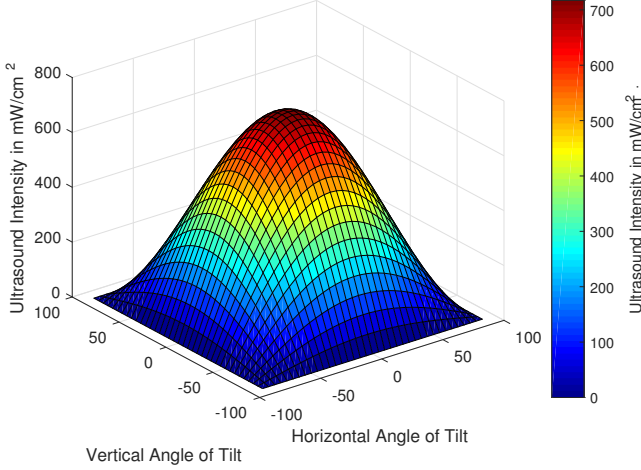


Fig. 5: Plot of Ultrasound Intensity vs Angles of Tilt for a frequency of 50kHz and a skin/fat depth of 5 mm. The tilting of the nanodevice will have a significant impact on the incident ultrasound intensity.

Thus, a $1000\mu\text{m}^2$ ultrasound harvesting nanodevice with 20 nanowires per μm^2 at a depth of 1 cm and incident ultrasound intensity of 710 mW/cm^2 (input work per nanowire of 7.1 fJ) could have a power output of 39 nW when a conversion factor of 0.55% is used.

The voltage output of a nanodevice depends on the magnitude of bending that the nanowires experience. In order to drive any microelectronic circuitry, a voltage level of between -0.2 V and -0.3 V would be necessary. As indicated in Table I the theoretical output voltage of a nanowire bent by a force of 80 nN is -0.284 V, but experimental results for the same bending force provide a voltage level of -25 mV [19] (less than 10% of the theoretical values), although this divergence is partly because of the difficulty in measuring at the nanoscale. By conservatively reducing the expected output voltage at 80 nN from -0.284 V to -0.025 V while retaining the same magnitude of bending, we can use (8) to calculate a new constant G' and derive new values of output voltage (V_o) for each value of force and bending.

$$V_o = G' y_m \quad (8)$$

This will give us the value of G' as $1.712 \times 10^{-4}\text{ V/nm}$. We then use this scaling to calculate the output voltage and current of a $1000\mu\text{m}^2$ nanodevice when subjected to increasing intensity of incident ultrasound energy. From (2) we can derive the relationship between the amount of bending in the wire (y_m) and the energy needed for bending (ΔE) as follows:

$$y_m = \sqrt{\frac{\Delta E 2L^3}{3YI}}. \quad (9)$$

We also know from (5), the amount of energy per nanowire that a specific intensity of ultrasound can deliver (E_{nw}). By substituting for ΔE and also using (8), we can derive the relationship between the output voltage (V_o) and incident ultrasound intensity (U_r) for a nanowire as follows:

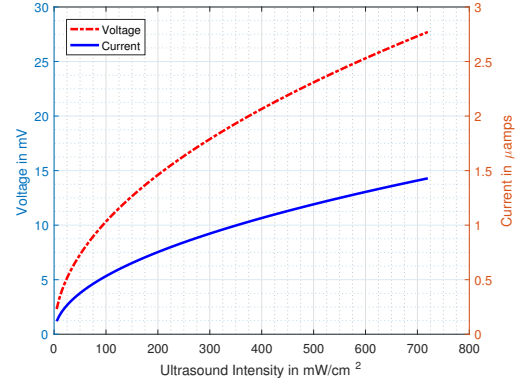


Fig. 6: Plot of ultrasound intensity against output voltage and output current for a $1000\mu\text{m}^2$ nanodevice at an ultrasound frequency of 50kHz.

$$\begin{aligned} V_o &= G' y_m \\ &= G' \sqrt{\frac{\Delta E 2L^3}{3YI}} \\ &= G' \sqrt{\frac{2L^3}{3YImK}} \sqrt{U_r}. \end{aligned} \quad (10)$$

The nanowire size, the density of nanowires (m) and the ultrasound frequency (K) are all fixed so the only variables are the voltage level V_o and the incident ultrasound intensity U_r . The maximum current output of a nanodevice depends on the total charge generated from all the bent nanowires and how quickly the charge is released. In our model we calculate the output current I_o from the output power P_o and voltage V_o :

$$I_o = \frac{P_o}{V_o} = \frac{AU_r e}{V_o}. \quad (11)$$

The resulting plots of nanodevice output voltage and current against ultrasound intensity, based on (10) and (11) are shown in Fig. 6. The plots are approximately linear except at lower levels of the ultrasound intensity.

In summary, for a successful operation of ultrasound energy harvesting, the conditions that need to be considered are:

- The nanodevices should all be at the same depth.
- There should be no denser tissue or bone obstructing the path in order to minimise absorption and reflections.
- The nanodevices should be inserted so as to minimise any tilt in order to collect the maximum ultrasound intensity.

Having determined the output voltage and current levels for an ultrasound-harvesting embedded nanodevice, we now examine the current and voltage levels needed to stimulate peripheral nerves in the human body.

IV. NEURON ACTIVATION

The human nervous system has two broad divisions: (i) the peripheral nervous system providing sensing and muscle activation (motor) functions throughout the human body and (ii) the central nervous system (the brain and spinal cord) for

processing sensory information and sending control signals to/from the peripheral nervous system. The nervous system has two main types of cells: neurons for communications and glial cells for support and nutrition. Neurons have a resting potential, based on an ionic balance of sodium and potassium ions across the neural membrane, of approximately -70 mV. If a stimulus raises this potential above -55 mV (e.g., by applying a pulse of magnitude 15 mV or greater) then the neuron activates, where ion channels in the membrane open and positively charged sodium ions flow across the membrane into the neuron (depolarisation). The potential rapidly increases to about 40 mV (a total increase of 110 mV from rest). At this point the sodium ion channels close, potassium ion channels open and there's a flow of positive potassium ions out of the neuron (repolarisation) [20].

The electrical signal (action potential) then propagates down the neuron's axon and either transfers to another neuron (via neurotransmitters) or a muscle cell, for example. The first neuron then returns to the rest state. The whole cycle takes between 5 ms and 10 ms. A stimulus can be supplied as part of the normal functioning of the nervous system or as an externally induced electrical current. External pulses are usually supplied by *cathodic* stimulation where a negative electrode is placed outside the cell membrane. The negative potential outside the membrane induces a current that reduces the trans-membrane voltage (depolarises) and will trigger an action potential if the stimulus current and the resulting change in membrane potential is large enough.

The level of current needed to stimulate a neuron will depend on the excitability of the neuron, the electrode-neuron distance and the pulse duration. Larger diameter axons are more excitable and require lower stimulus energy than smaller diameters. Such larger axons have an insulating sheath of *myelin* and are classed as $A\alpha$, $A\beta$ and $A\delta$. The myelin sheath has regular gaps at intervals of 1 mm, called nodes of Ranvier (typical width of 2 μm) where the action potential is regenerated. These nodes are also the points at which an external stimulus pulse will enter the neuron.

The electrode voltage and the associated source current are important input values needed in order to determine the resultant currents and voltages induced in the neuron. Numerous research works have modeled the excitation of neurons using monopolar electrodes [21], [22], [23]. In particular, we are interested in determining the magnitude of a stimulus current that triggers an action potential, the electrode voltage needed to drive that current and the electrode position. This will allow us to determine the appropriate current and voltage required from the nanodevices to stimulate the neurons in the nerve. The calculation of stimulus current values using experimentally derived empirical equations is described in the next section.

A. Activation Parameters

The effect of the stimulus can be varied by increasing or decreasing the pulse length and hence influencing the activation of neurons of different size and depth in the nerve bundle. The lowest possible stimulus current of an axon is called the *rheobase* but this implies an infinitely long pulse

TABLE II: Axon Characteristics

Axon Type	Myelin	Diameter (μm)	Speed (m/s)	Chronaxie (μs)
$A\alpha$	Yes	13-20	80-120	50-100
$A\beta$	Yes	6-12	35-75	120
$A\delta$	Yes	1-5	10-35	170
B	Yes	3	3-15	200
C	No	0.2-1.5	0.5-2.0	400

[24]. The rheobase is usually measured at the source electrode. Due to the tissue resistivity, the rheobase will be higher when the electrode is placed at a certain distance (e.g., on the skin). A more usual parameter is the *chronaxie*, the minimum time required for a stimulus current that's twice the value of the rheobase to stimulate a neuron [24]. Factors affecting the accuracy of chronaxie measurements are discussed by Geddes [25] who notes that the most reliable values are obtained when a square stimulus pulse is used. Axon characteristics, including their chronaxie value for different types of neurons are summarised in Table II.

The source current intensity for stimulation must be increased as the distance between the electrode and the neuron increases. The increase in source current intensity with distance is defined by the current-distance equation [24], which is represented as:

$$I_d = I_{th} + kd^2. \quad (12)$$

The minimum threshold current for neuron activation at zero distance is I_{th} . At a distance d , the activation current intensity is I_d and the current-distance constant is k which is specific for different types of axon. Values of k were analysed by Ranck [26] for a wide range of axon types and measured by varying methods. A more accurate method of determining the value for a peripheral motor neuron was devised by Mahman et al. [27] who also calculated a value for the threshold current I_{th} . In our modelling we use this calculated current-distance constant k of 27 $\mu\text{A}/\text{mm}^2$.

The pulse duration and the corresponding threshold pulse current intensity for neural activation can be plotted using the Lapicque equation [24], which is represented as:

$$I_{th} = I_r \left(1 + \frac{C}{t}\right). \quad (13)$$

where the pulse duration is t , the rheobase current is I_r and the chronaxie is C . The shorter the pulse duration, the higher the threshold intensity needed to activate a neuron. The optimum pulse duration for a specific neuron is the chronaxie. A plot of pulse duration against current intensity (I_{th}), based on (13), for a myelinated and unmyelinated axon is shown in Fig. 7. For an electrode in very close proximity to a nerve we model a rheobase current of 25 μA that's derived from Mahman's value of threshold current (50 μA) and a pulse length of 100 μs .

If we consider a pulse length of 100 μs then we can see from Fig. 7 that the different axon types could be activated by a stimulus current of less than 0.2 mA.

The magnitude of the stimulus current will also depend on the voltage at the electrode. For a monopolar electrode the

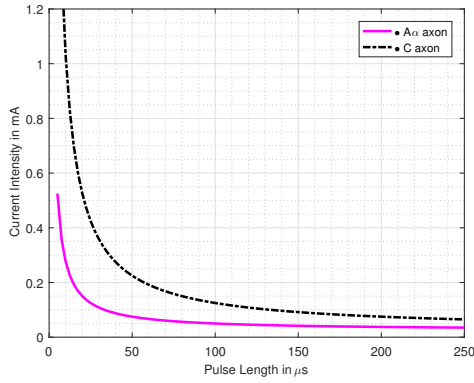


Fig. 7: Plot of current against pulse duration for two types of axon, one myelinated ($A\alpha$ axon) and one unmyelinated (C axon). The current intensity for a pulse duration of $100\mu s$ is less than 0.2 mA.

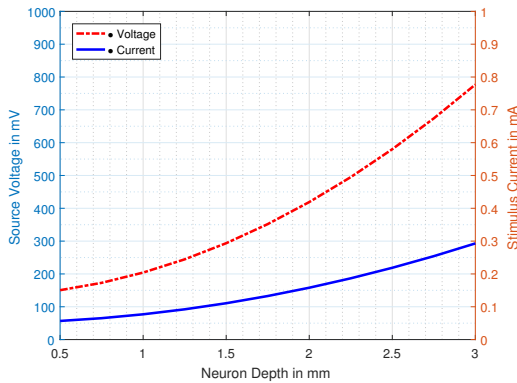


Fig. 8: Plot of stimulus current and source voltage for a range of neuron distances and a chronaxie of $100\mu s$. The further the neuron is from the nanodevice array electrode the higher will be the required stimulus voltage/current.

electrical potential field V_u at a distance u is given by the following equation [24] :

$$V_u = \frac{I_d}{4\pi\rho u}. \quad (14)$$

The stimulus current intensity is I_d while the conductivity of the extracellular tissue is ρ . If we assume a homogenous tissue then we can assign a specific value to the conductivity. A typical value for neuronal tissue conductivity is 0.3 S/m [28]. The potential at zero distance is infinite so some specific radius has to be assigned to the electrode in order to provide a minimum value of u and allow for a realistic source voltage [29]. Therefore, due to this factor we assign a radius of 0.1 mm. Fig. 8 shows the variation in stimulus current and source electrode voltage with neuron depth for a neuron with a chronaxie of $100\mu s$ stimulated by a $100\mu s$ pulse.

Values for electrode voltage and stimulus current, derived from (12) and (14) for a range of neuron depths are shown in Table III. These values are comparable to experimental and modelling results for cuff electrode stimulation of peripheral nerves [30].

TABLE III: Electrode voltage and stimulus current for a range of neuron depths.

Neuron Depth (mm)	Electrode Voltage (mV)	Stimulus Current (mA)
0.5	150.5	0.057
1	204	0.077
1.5	293	0.11
2	419	0.158
2.5	580	0.219
3	777	0.293

The optimum position for a stimulating electrode is at a node of Ranvier but it is possible to trigger an action potential between nodes if the stimulus is strong enough. The stimulus current and corresponding electrode voltage are the key parameters that our energy-harvesting nanodevices must provide in order to stimulate neurons at different depths. We now examine the properties of specific peripheral nerves that we wish to stimulate.

B. Peripheral Nerve Bundles

Peripheral nerves have neurons grouped in bundles (fascicles) within a nerve and so it is difficult to trigger a specific neuron.

The peripheral nerves of the wrist and forearm that control arm and hand movements are the *radial*, *median* and *ulnar*. At the wrist and elbow, these nerves are buried beneath a layer of skin/fat (between 1 cm and 1.5 cm) and hence are easily accessed [31]. The cross-sectional areas of the nerves vary between 5 mm² and 10 mm² [32]. There has been some research in mapping the topography of fascicles through the median, radial and ulnar nerves by Jabaley et al. [33] and Stewart [34]. These studies showed (i) the position of a fascicle could change within a nerve particularly after the nerve had branched and (ii) that key fascicles contained neurons of one type only (either motor or sensory). An accurate mapping of motor neurons to fascicles would provide valuable information for the placement of the nanodevices and the calculation of the probability of stimulating a particular neural response. A distribution of motor and sensory fascicles in the median nerve, based on [33] and [34], is shown in Fig. 9.

We model the median nerve as having an elliptical cross-section with a major diameter of 6 mm, a minor diameter of 2 mm, a cross-sectional area of 9.5 mm² and a perimeter of 13.4 mm. If a stimulating electrode is placed at the mid-point on the top surface of such a nerve then the radial distance from this point to the relevant fascicle will determine the level of stimulating current needed. However, if the motor fascicles are concentrated on one side of the nerve then the electrode should be placed on that side of the nerve to avoid stimulating other sensory fascicles. Examples of electrode placement on the median nerve at the wrist and elbow are shown in Fig. 9. In both cases the electrodes are placed to maximise access to the motor neuron fascicles and the stimulating current can be set to penetrate to the radial distances shown.

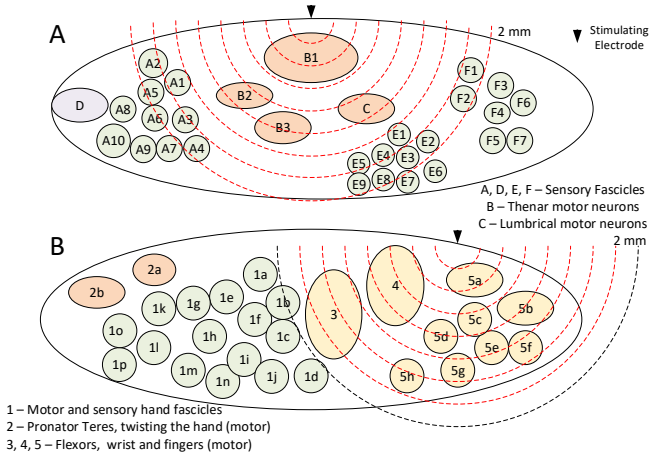


Fig. 9: Schematic diagram of median nerve fascicles at the wrist (A) and the elbow (B), showing how electrode placement can concentrate the stimulating current on groups of motor fascicles.

C. Nanodevice Neural Activation

A neuron's axon can be stimulated at any point along its length by an electrical pulse of sufficient magnitude. An activating nanodevice must (i) have sufficient voltage and charge for stimulation and (ii) allow for an interval of 10 ms between discharges. In theory, a neuron could be activated 100 times per second but this would be considered a very high rate. Activation rates of 10 or less per second are more usual. Nerve stimulus currents are usually in the mA range (see Fig. 8), though the closer the stimulating electrode can be placed to the nerve then the lower the requirement. Our modelled nanodevices have a maximum voltage level of tens of mV and produce current in the μA range (see Fig. 6). *Therefore, based on these requirements, the nanodevices must be coupled together in parallel to increase the current and in series to increase the voltage.* The coupling of individual ultrasound harvesting nanodevices in series to boost voltage output and in series to boost current output is described by Wang in [19]. The experimental results show that the voltages and currents add as a linear superposition when the ultrasound is activated. The nanodevices should be capable of delivering square-wave pulses of varying duration across two electrodes, a cathode of coupled zigzag electrodes and an anode of coupled substrates, that can in turn stimulate a nerve.

The minimum possible pulse length from a nanodevice driven by a 50 kHz ultrasound signal is $20 \mu\text{s}$. A longer stimulation time will contain a train of such pulses. The in-built rectification and capacitive properties of the nanogenerator convert this train to a single square-wave DC pulse. Neural stimulation systems usually provide some form of charge balancing, delivering a biphasic pulse of cathodic current followed by anodic current. The claimed benefit is to minimize the degrading effects of charge build-up on the electrode and surrounding tissue. Our system is a passive device array and can only provide monophasic cathodic pulses. It cannot switch to biphasic operation or produce more complex stimulation

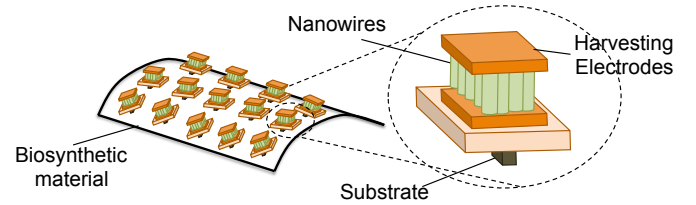


Fig. 10: Schematic diagram of coupled nanodevices embedded in a patch of synthetic biocompatible tissue.

patterns.

The method of inserting nanodevices in close proximity to neurons then becomes an important factor. We propose encasing an array of coupled nanodevices within a sealed patch of synthetic tissue, as illustrated in Fig. 10, and then inserting the patch of tissue at the site. The use of coupled arrays and bio-compatible packaging ensures that the individual nanodevices do not interact with the nerve or nerve fascicle but only act through a single cathode/anode system. The bio-compatible material provides insulation for the array in the surrounding conductive environment.

D. Patch Dimensions

The nanodevice array must deliver a current intensity (I_d) in accordance to (12). That intensity in turn is also dependent on the pulse duration as shown in (13). If the output current level of a nanodevice at a particular ultrasound intensity is I_o , and the threshold stimulus current for a particular neuron depth is I_d , then the number of rows of coupled nanodevices to generate the threshold current is:

$$N_r = \frac{I_d}{I_o}. \quad (15)$$

The voltage must also be in the range specified by (14) and calculated for an electrode radius of 0.1 mm. If the output voltage of a nanodevice at particular ultrasound intensity is V_o , and the electrode voltage for a particular threshold current is V_e , then the number of columns of coupled nanodevices to generate the threshold voltage is:

$$N_c = \frac{V_e}{V_o}. \quad (16)$$

The median and ulnar nerves are contained in a skin/fat depth between 1 cm and 1.5 cm. The external ultrasound intensity will have dropped below its initial intensity of 720 mW/cm^2 at these depths. Hence we use a maximum intensity of 710 mW/cm^2 with a maximum current and voltage per nanodevice of $1.42 \mu\text{A}$ and 27.5 mV. The minimum possible area of a patch of nanodevices, A_p will be derived from the number of rows N_r , the number of columns N_c and the area of one nanodevice a_n :

$$A_p = N_r N_c a_n. \quad (17)$$

The basic length and width of an array of nanodevices are set by the number of rows and columns. Our nanodevices are $1000 \mu\text{m}^2$ and can be modelled as squares of side $32 \mu\text{m}$. There will be a need to allow for small variations in

TABLE IV: Array dimensions for neuron activation at specific depths and a constant ultrasound intensity of 710 mW/cm².

Depth (mm)	Length (mm)	Width (mm)	Fascicles
1	2.16	0.28	5a, 5c ,4, B1
1.5	3.12	0.55	5b, 5d, 5e, 5f, 5g, 4, B2, B3, C
2	4.44	0.6	5h, 3, A1, A2, A3, A4, A5, F1, F2, E1, E2, E3, E4, E5, E8, E9
2.5	6.16	0.84	1a,1b, 1c, 1d, 1f, A6, A7, A8, A9, F3, F4, F5, F6, E6, E7
3	8.24	1.12	1e, 1g, 1h, 1i, 1j, F7, A10, D

dimension as well as a space for coupling connections between the devices. We, therefore, increase the effective size of a nanodevice to 40 μm per side, giving an effective area of 1600 μm^2 . A plot of minimum array area for a range of neuron depths, pulse durations and input ultrasound intensity is shown in Fig. 11. The plots show how the area increases for greater stimulus depth and shorter pulse lengths, since both of these will result in higher current and voltage. The area decreases for higher ultrasound intensity as each device can produce more current and voltage.

Nanodevice array dimensions of length and width are based on translating the number of rows and columns into equivalent dimensions in millimetres. For example, at a depth of between 1 cm and 1.5 cm there would be an ultrasound intensity of 710 mW/cm² with a maximum individual nanodevice voltage of 27.5 mV and current of 1.42 μA . It would require 73 nanodevices in series to deliver 2 V and 141 nanodevices in parallel to deliver 200 μA , giving an array of 3 mm by 5.64 mm or 16.92 mm². It is possible to subdivide the rows and columns into coupled blocks in order to increase the width and reduce the length of an array. The block coupling would preserve nanodevice parallel and series wiring but would extend some connections to allow the rearrangement of blocks in the array. The maximum possible width of the array is half the circumference of the nerve or fascicle that the array will be placed on.

E. Selectivity of Activation

A fixed-size array of nanodevices can be designed to stimulate the deepest motor neurons but in doing so the current will also stimulate all closer motor neurons. Some degree of depth selectivity can be engineered by (i) using a variable-width ultrasound beam that can irradiate different parts of an array and (ii) reducing the incident ultrasound intensity over the full array.

When the ultrasound beam is directed at smaller areas of an array, then lower intensity stimulus pulses can be generated. We consider an array, for example, with sufficient rows and columns to stimulate motor neurons at a maximum depth of 3 mm at maximum ultrasound intensity. The sub- area (length and width) that needs to intercept ultrasound energy for different depths of neuron stimulation is shown in Table IV. The *additional* fascicles stimulated at each depth are also shown based on the distribution in Fig. 9.

Reducing the intensity of an ultrasound beam on a fixed array size will also reduce the resultant current and voltage

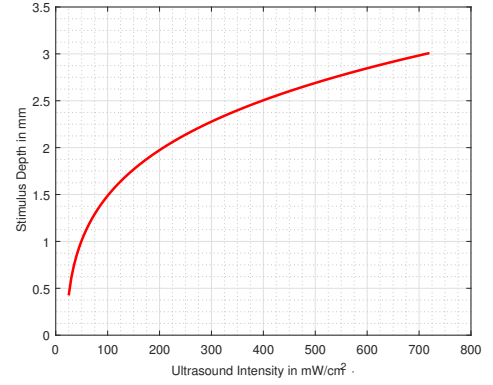


Fig. 12: Plot of Ultrasound Intensity vs. Stimulus Depth for a fixed-size array (8.24 mm length, 1.12 mm width) of nanodevices.

and hence the stimulus depth. The stimulus depth d can be expressed as a function of stimulus current I_d by rearranging (12).

$$d = \sqrt{\frac{I_d - I_{th}}{k}} \quad (18)$$

The stimulus current (I_d) in turn can be expressed as a function of ultrasound intensity (U_r) by combining (15), (11) and substituting in (18). The number of rows of nanodevices is N_r , the area of a nanodevice is A , the output efficiency is e and the output voltage of a nanodevice is V_o .

$$\begin{aligned} d &= \sqrt{\frac{(N_r I_o) - I_{th}}{k}} \\ &= \sqrt{\frac{(N_r A e U_r) - I_{th} V_o}{k V_o}}. \end{aligned} \quad (19)$$

The effect of reducing the ultrasound intensity on a fixed-size horizontal array is shown in Fig. 12. The array is dimensioned to stimulate neurons at a depth of 3 mm when subjected to an ultrasound intensity of 710 mW/cm². The reduction in ultrasound intensity U_r causes a reduction in stimulus current I_d with a corresponding reduction in stimulus depth d .

The most difficult fascicle targeting to achieve is to stimulate a deep fascicle without stimulating closer fascicles. The only method for achieving this in limited circumstances is the generation of sub-threshold stimulus pre-pulses as described by Grill and Mortimer [35]. These pre-pulses can temporarily raise the stimulus threshold of the closest fascicle allowing a follow-on to stimulate a deeper fascicle. However pulse timing, pulse length and pulse interval are crucial in implementing this.

A further degree of selectivity can be achieved by deploying multiple electrodes at different locations across a nerve surface. This would require either embedding separate patches or providing multiple arrays within a single patch. The stimulating electrodes would be positioned as close as possible to the target fascicles and engineered to deliver the stimulus current. The electrodes would be energised either singly simultaneously by the ultrasound beam and the system could be modelled as a multipole electrode with careful

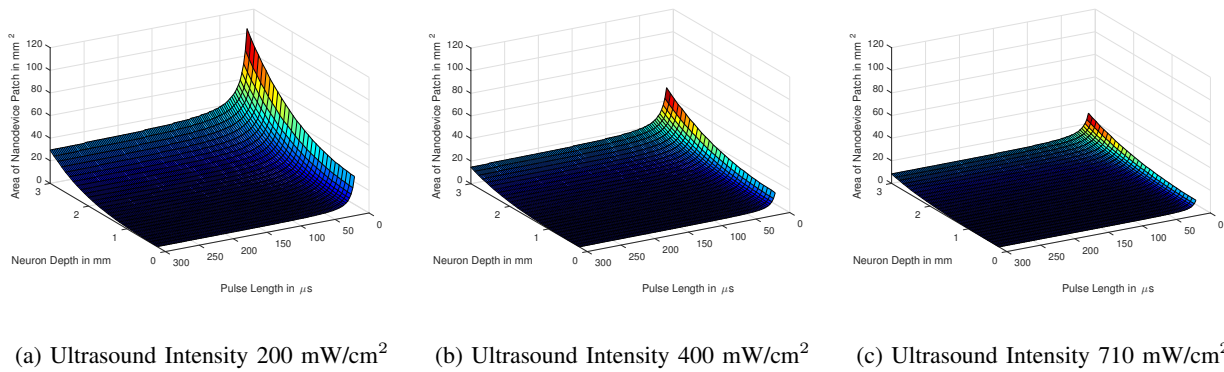


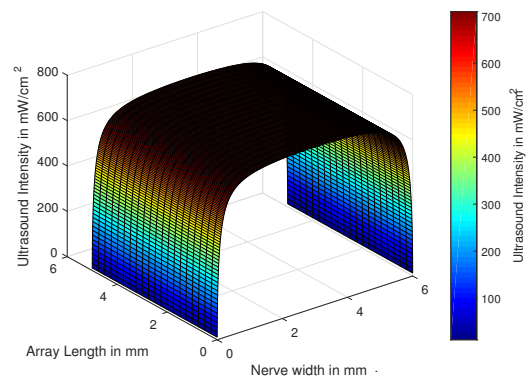
Fig. 11: Nanodevice array area for a range of neuron depths, pulse lengths and ultrasound intensities. The array area needs to be significantly larger if the incident ultrasound intensity is lower.

attention paid to interaction between the stimulus currents [36] [37]. The modelling of multiple patches or arrays will be a subject of further study.

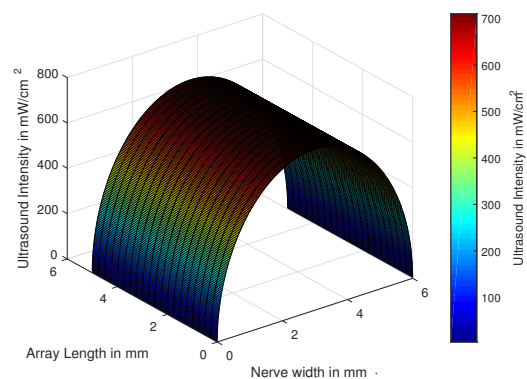
Examples of how an ultrasound intensity of 710 mW/cm² decreases from the centre to the edges of an elliptical nerve and a circular nerve are shown in Fig. 13. The modelled surface segment of the nerve has a major axis (ellipse) or diameter (circle) of 6 mm and a length of 5 mm. The reduction in incident ultrasound intensity on a curved patch will cause a reduction in stimulus current and stimulus depth. The actual reduction will depend on how much of the patch rests on the curved edge of the nerve surface. In both cases the maximum intensity occurs on the part of the nerve surface that is normal or near-normal to the incident beam (e.g., the midpoint). As the angle of curvature increases, the intensity decreases but the effect is more pronounced on a circular cross-section. This suggests that the width of a nanodevice array, or the deployment of multiple arrays, must be tailored to the type of nerve (elliptical or circular cross-section) in order to maximise energy harvesting.

V. CONCLUSION

We have shown that an external ultrasound portable source can be a viable method for supplying wireless vibrational energy to an embedded patch of energy-harvesting nanodevices. The harvesting is implemented with non-resonant piezoelectric *ZnO* nanowires that allow the use of lower-frequency ultrasound (50kHz) with a lower absorption loss in human tissue. The intensity of the ultrasound must remain within safe medical limits and there must be no air gap between the source and the human skin. By coupling the nanodevices into an array we can boost the power output and emulate an electrode for peripheral nerve stimulation. The size of the array, the area activated and the intensity of the ultrasound can all be varied in order to provide a certain element of selective neural activation. In the future, such stimulation will have a greater role in treating debilitating neural conditions, compensating for nerve damage and enhancing prosthetic control. This would entail the deployment of such nanodevice arrays not only in the peripheral nervous system but also in the central nervous system and possibly on the surface



(a) Elliptical cross-section.



(b) Circular cross-section.

Fig. 13: Ultrasound intensity across (a) an elliptical cross-section nerve (major axis 6mm) and (b) a circular cross-section nerve (diameter 6mm).

of the brain. The wireless nanodevice patch could also be utilised to communicate through the nervous system itself by generating action potentials to send data messages to distant receivers. This will enable the nervous system to be used as an information highway to communicate between multiple nanodevices that are interfaced to the nerves. Embedded energy-

harvesting nanodevices may also acquire increased functionality for directing targeted drug delivery and sensing of medical conditions through molecular communications [38]. Networks of nanodevices could be established in the skin or in specific organs such as the heart in order to detect changes in key chemical concentrations and communicate this information to an external monitoring system. Once this communication subsystem of the nervous system is interconnected to the Internet using, for example, terahertz communications [39] we can then realize the vision of the Internet of Bio-Nano Things [40].

REFERENCES

- [1] J. T. Mortimer and N. Bhadra, *Peripheral Nerve and Muscle Stimulation*. World Scientific Pub, 2004, ch. 4.2, pp. 638–682.
- [2] D. B. Popovic, “Advances in functional electrical stimulation (fes),” *Journal of Electromyography and Kinesiology*, vol. 24, no. 6, pp. 795 – 802, 2014.
- [3] N. S. Korivi and P. K. Ajmera, “Clip-on micro-cuff electrode for neural stimulation and recording,” *Sensors and Actuators B: Chemical*, vol. 160, no. 1, pp. 1514 – 1519, 2011.
- [4] S. F. Cogan, “Neural stimulation and recording electrodes,” *Annual Review of Biomedical Engineering*, vol. 10, no. 1, pp. 275–309, 2008, PMID: 18429704.
- [5] M. Capogrosso, T. Milekovic, D. Borton, F. Wagner, E. M. Moraud, J.-B. Mignardot, N. Buse, J. Gandar, Q. Barraud, D. Xing, E. Rey, S. Duis, Y. Jianzhong, W. K. D. Ko, Q. Li, P. Detemple, T. Denison, S. Micera, E. Bezar, J. Bloch, and G. Courtine, “A brain-spine interface alleviating gait deficits after spinal cord injury in primates,” *Nature*, vol. 539, no. 7628, pp. 284–288, 11 2016.
- [6] Y. Qin, M. M. Howlader, M. J. Deen, Y. M. Haddara, and P. R. Selvaganapathy, “Polymer integration for packaging of implantable sensors,” *Sensors and Actuators B: Chemical*, vol. 202, pp. 758 – 778, 2014.
- [7] M. Donohoe, S. Balasubramaniam, B. Jennings, and J. M. Jornet, “Powering in-body nanosensors with ultrasounds,” *IEEE Transactions on Nanotechnology*, vol. 15, no. 2, pp. 151–154, March 2016.
- [8] S. Ozeri and D. Shmilovitz, “Ultrasonic transcutaneous energy transfer for powering implanted devices,” *Ultrasonics*, vol. 50, no. 6, pp. 556 – 566, 2010.
- [9] P. J. Larson and B. C. Towe, “Miniature ultrasonically powered wireless nerve cuff stimulator,” in *2011 5th International IEEE/EMBS Conference on Neural Engineering*, April 2011, pp. 265–268.
- [10] D. Seo, J. M. Carmena, J. M. Rabaey, M. M. Maharbiz, and E. Alon, “Model validation of untethered, ultrasonic neural dust motes for cortical recording,” *Journal of Neuroscience Methods*, vol. 244, pp. 114 – 122, 2015, brain Computer Interfaces; Tribute to Greg A. Gerhardt.
- [11] D. Seo, R. Neely, K. Shen, U. Singhal, E. Alon, J. Rabaey, J. Carmena, and M. Maharbiz, “Wireless recording in the peripheral nervous system with ultrasonic neural dust,” *Neuron*, vol. 91, no. 3, pp. 529 – 539, 2016. [Online]. Available: <http://www.sciencedirect.com/science/article/pii/S0896627316303440>
- [12] Y. Gao and Z. L. Wang, “Electrostatic potential in a bent piezoelectric nanowire. the fundamental theory of nanogenerator and nanopiezotronics,” *Nano Letters*, vol. 7, pp. 2499–2505, 2007.
- [13] R. Hinchet, J. Ferreira, J. Keraudy, G. Ardila, E. Pauliac-Vaujour, M. Mouis, and L. Montes, “Scaling rules of piezoelectric nanowires in view of sensor and energy harvester integration,” in *IEEE International Electron Devices Meeting (IEDM), 2012*, Dec 2012, pp. 6.2.1–6.2.4.
- [14] Z. L. Wang and J. Song, “Piezoelectric nanogenerators based on zinc oxide nanowire arrays,” *Science*, vol. 312, no. 5771, pp. 242–246, 2006.
- [15] X. Wang, J. Song, J. Liu, and Z. L. Wang, “Direct-current nanogenerator driven by ultrasonic waves,” *Science*, vol. 316, no. 5821, pp. 102–105, 2007.
- [16] X. Wang, J. Liu, J. Song, , and Z. L. Wang, “Integrated nanogenerators in biofluid,” *Nano Letters*, vol. 7, no. 8, pp. 2475–2479, 2007, PMID: 17604406.
- [17] W. R. Hendee and E. R. Ritenour, *Ultrasound Waves*. John Wiley & Sons, Inc., 2003, pp. 303–316.
- [18] X. Wang, Y. Gao, Y. Wei, and Z. Wang, “Output of an ultrasonic wave-driven nanogenerator in a confined tube,” *Nano Research*, vol. 2, no. 3, pp. 177–182, 2009.
- [19] Z. L. Wang, “Towards self-powered nanosystems: From nanogenerators to nanopiezotronics,” *Advanced Functional Materials*, vol. 18, no. 22, pp. 3553–3567, 2008.
- [20] J. Malmivuo and R. Plonsey, *Bioelectromagnetism - Principles and Applications of Bioelectric and Biomagnetic Fields*. Oxford University Press, 1995, ch. 2, pp. 33 – 42.
- [21] S. L. BeMent and J. B. R. Jr., “A model for electrical stimulation of central myelinated fibers with monopolar electrodes,” *Experimental Neurology*, vol. 24, no. 2, pp. 171 – 186, 1969.
- [22] D. R. McNeal, “Analysis of a model for excitation of myelinated nerve,” *IEEE Transactions on Biomedical Engineering*, vol. BME-23, no. 4, pp. 329–337, July 1976.
- [23] F. Rattay, “Current distance relations for fiber stimulation with pointsources,” *IEEE Transactions on Biomedical Engineering*, vol. 55, no. 3, pp. 1122–1127, March 2008.
- [24] D. T. Brocker and W. M. Grill, “Chapter 1 - principles of electrical stimulation of neural tissue,” in *Brain Stimulation*, ser. Handbook of Clinical Neurology, A. M. Lozano and M. Hallett, Eds. Elsevier, 2013, vol. 116, pp. 3 – 18.
- [25] L. A. Geddes, “Accuracy limitations of chronaxie values,” *IEEE Transactions on Biomedical Engineering*, vol. 51, no. 1, pp. 176–181, Jan 2004.
- [26] J. B. Ranck, “Which elements are excited in electrical stimulation of mammalian central nervous system: A review,” *Brain Research*, vol. 98, no. 3, pp. 417 – 440, 1975.
- [27] A. Mahnam, S. M. R. Hashemi, and W. M. Grill, “Measurement of the current distance relationship using a novel refractory interaction technique,” *Journal of Neural Engineering*, vol. 6, no. 3, p. 036005, 2009.
- [28] S. Joucla and B. Yvert, “Modeling extracellular electrical neural stimulation: From basic understanding to mea-based applications,” *Journal of Physiology-Paris*, vol. 106, pp. 146 – 158, 2012, neuronal Ensemble Recordings in Integrative Neuroscience.
- [29] D. M. Durand, W. M. Grill, and R. Kirsch, *Electrical Stimulation of the Neuromuscular System*. Boston, MA: Springer US, 2005, pp. 157–191.
- [30] K. H. Polasek, H. A. Hoyen, M. W. Keith, and D. J. Tyler, “Human nerve stimulation thresholds and selectivity using a multi-contact nerve cuff electrode,” *IEEE Transactions on Neural Systems and Rehabilitation Engineering*, vol. 15, no. 1, pp. 76–82, March 2007.
- [31] R. McCahon and N. Bedforth, “Peripheral nerve block at the elbow and wrist,” *Continuing Education in Anaesthesia, Critical Care & Pain*, vol. 7, no. 2, pp. 42–44, 2007.
- [32] B. Mani, R. Sarawagi, and R. A. Cherian, “Review of the dimensions of the median nerve and carpal tunnel using sonography in asymptomatic adults,” *Journal of Medical Imaging and Radiation Oncology*, vol. 55, no. 2, pp. 126–131, 4 2011.
- [33] M. E. Jabaley, W. H. Wallace, and F. R. Heckler, “Internal topography of major nerves of the forearm and hand: A current view,” *The Journal of Hand Surgery*, vol. 5, no. 1, pp. 1 – 18, 1980.
- [34] J. D. Stewart, “Peripheral nerve fascicles: Anatomy and clinical relevance,” *Muscle & Nerve*, vol. 28, no. 5, pp. 525–541, 2003.
- [35] W. M. Grill and J. T. Mortimer, “Stimulus waveforms for selective neural stimulation,” *IEEE Engineering in Medicine and Biology Magazine*, vol. 14, no. 4, pp. 375–385, Jul 1995.
- [36] J. D. Sweeney, D. A. Ksienski, and J. T. Mortimer, “A nerve cuff technique for selective excitation of peripheral nerve trunk regions,” *IEEE Transactions on Biomedical Engineering*, vol. 37, no. 7, pp. 706–715, July 1990.
- [37] M. D. Tarler and J. T. Mortimer, “Selective and independent activation of four motor fascicles using a four contact nerve-cuff electrode,” *IEEE Transactions on Neural Systems and Rehabilitation Engineering*, vol. 12, no. 2, pp. 251–257, June 2004.
- [38] B. Atakan, S. Galmes, and O. B. Akan, “Nanoscale communication with molecular arrays in nanonetworks,” *IEEE Transactions on NanoBioScience*, vol. 11, no. 2, pp. 149–160, June 2012.
- [39] G. Piro, K. Yang, G. Boggia, N. Chopra, L. A. Grieco, and A. Alomainy, “Terahertz communications in human tissues at the nanoscale for healthcare applications,” *IEEE Transactions on Nanotechnology*, vol. 14, no. 3, pp. 404–406, May 2015.
- [40] I. Akyildiz, M. Pierobon, S. Balasubramaniam, and Y. Koucheryavy, “The internet of bio-nano things,” *IEEE Communications Magazine*, vol. 53, no. 3, pp. 32–40, March 2015.



Michael Donohoe (M16) is a PhD student in the Telecommunications Software and Systems Group (TSSG) of the Waterford Institute of Technology, Ireland. He graduated from University College Galway, Ireland, in 1980 with a BSc in Physics. He has worked in the telecommunications industry especially in the areas of network planning, project implementation, R&D and product management. His research interests include embedded nanodevices, energy harvesting and in-body communications networks.



Sasitharan Balasubramaniam (SM14) received his Bachelor (Electrical and Electronic Engineering) and Ph.D. degrees from the University of Queensland in 1998 and 2005, respectively, and Masters (Computer and Communication Engineering) degree in 1999 from the Queensland University of Technology. He is currently an Academy of Finland Research Fellow at the Nano Communication Centre, Department of Electronic and Communication Engineering, Tampere University of Technology, Finland, and Acting Director of Research at the Telecommunication Software and Systems Group, Waterford Institute of Technology, Ireland, where he worked on a number of Science Foundation Ireland projects. He has published over 90 papers and actively participates in a number of technical programme committee for various conferences. Sasitharan was the TPC co-chair for ACM NANOCOM 2014 and General Chair in 2015 which he co-founded. He is currently an editor for the IEEE Internet of Things journal, Elsevier Nano Communication Networks, and Elsevier Digital Communication Networks. His current research interests includes bio-inspired communication networks, as well as molecular communications. Sasitharan is an IEEE Senior member.



Brendan Jennings (M05) received the BEng and PhD degrees from Dublin City University, Ireland, in 1993 and 2001, respectively. He is a Principal Investigator with CONNECT, Ireland's national research centre for future networks and communications, leading a team of researchers based at the Telecommunications Software & Systems Group at Waterford Institute of Technology. He has spent periods as a Visiting Researcher with the KTH Royal Institute of Technology, Stockholm, Sweden, and in EMC² Research Europe, Cork, Ireland. He

regularly serves on the organization and technical program committees of a number of network and service management related conferences. He is the Executive Chair for IEEE ICC 2020, which will be hosted in Dublin, Ireland. His research interests include network management, edge computing in the Internet of Things, and nanoscale communications.



Josep Miquel Jornet (M13) is an Assistant Professor with the Department of Electrical Engineering at the University at Buffalo, The State University of New York. He received the B.S. in Telecommunication Engineering and the M.Sc. in Information and Communication Technologies from the Universitat Politècnica de Catalunya, Barcelona, Spain, in 2008. He received the Ph.D. degree in Electrical and Computer Engineering from the Georgia Institute of Technology (Georgia Tech), Atlanta, GA, in 2013. From September 2007 to December 2008, he was

a visiting researcher at the Massachusetts Institute of Technology (MIT), Cambridge, under the MIT Sea Grant program. He was the recipient of the Oscar P. Cleaver Award for outstanding graduate students in the School of Electrical and Computer Engineering, at Georgia Tech in 2009. He also received the Broadband Wireless Networking Lab Researcher of the Year Award in 2010. In 2016 and 2017, he received the Distinguished TPC Member Award at the IEEE International Conference on Computer Communications (INFOCOM). In 2017, he received the IEEE Communications Society Young Professional Best Innovation Award. Since July 2016, he is the Editor-in-Chief of the Nano Communication Networks (Elsevier) Journal. He also serves in the Steering Committee of the ACM Nanoscale Computing and Communications Conference series since 2016. He is a member of the IEEE and the ACM. His current research interests are in Terahertz-band communication networks, Nano-photonic wireless communication, Intra-body Wireless Nanosensor Networks and the Internet of Nano-Things.